

Investigating the temporal resolution limits of scintillation detection from pixellated elements:  
comparison between experiment and simulation

This article has been downloaded from IOPscience. Please scroll down to see the full text article.

2011 Phys. Med. Biol. 56 735

(<http://iopscience.iop.org/0031-9155/56/3/013>)

View [the table of contents for this issue](#), or go to the [journal homepage](#) for more

Download details:

IP Address: 171.65.80.217

The article was downloaded on 22/02/2011 at 00:35

Please note that [terms and conditions apply](#).

# Investigating the temporal resolution limits of scintillation detection from pixellated elements: comparison between experiment and simulation

V Ch Spanoudaki<sup>1,2</sup> and C S Levin<sup>1,2,3,4</sup>

<sup>1</sup> Molecular Imaging Program at Stanford (MIPS), Stanford University, Stanford, USA

<sup>2</sup> Department of Radiology, Stanford University School of Medicine, Stanford, USA

<sup>3</sup> Department of Electrical Engineering, Stanford University, Stanford, USA

<sup>4</sup> Department of Physics, Stanford University, Stanford, USA

E-mail: [cslevin@stanford.edu](mailto:cslevin@stanford.edu)

Received 28 September 2010, in final form 2 December 2010

Published 14 January 2011

Online at [stacks.iop.org/PMB/56/735](http://stacks.iop.org/PMB/56/735)

## Abstract

This study investigates the physical limitations involved in the extraction of accurate timing information from pixellated scintillation detectors for positron emission tomography (PET). Accurate physical modeling of the scintillation detection process, from scintillation light generation through detection, is devised and performed for varying detector attributes, such as the crystal element length, light yield, decay time and surface treatment. The dependence of light output and time resolution on these attributes, as well as on the photon interaction depth (DoI) of the annihilation quanta within the crystal volume, is studied and compared with experimental results. A theoretical background which highlights the importance of different time blurring factors for instantaneous ('ideal') and exponential ('realistic') scintillation decay is developed and compared with simulated data. For the case of a realistic scintillator, our experimental and simulation findings suggest that dependence of detector performance on DoI is more evident for crystal elements with rough ('as cut') compared to polished surfaces (maximum observed difference of 64% (25%) and 22% (19%) in simulation (measurement) for light output and time resolution, respectively). Furthermore we observe distinct trends of the detector performance dependence on detector element length and surface treatment. For short crystals ( $3 \times 3 \times 5 \text{ mm}^3$ ) an improvement in light output and time resolution for 'as cut' compared to polished crystals is observed (3% (7%) and 9% (9%) for simulation (measurement), respectively). The trend is reversed for longer crystals ( $3 \times 3 \times 20 \text{ mm}^3$ ) and an improvement in light output and time uncertainty for polished compared to 'as cut' crystals is observed (36% (6%) and 40% (20%) for simulation (measurement), respectively). The results

of this study are used to guide the design of PET detectors with combined time of flight (ToF) and DoI features.

(Some figures in this article are in colour only in the electronic version)

## 1. Introduction

Investigation of the timing properties of scintillator-based detectors has been a subject of extensive study in the field of positron emission tomography (PET) (Binkley 1994, Clinthorne *et al* 1990, Hero *et al* 1991, Moses and Ullisch 2006, Moszynski *et al* 1996, Petrick *et al* 1991, Post and Schiff 1950, Shao 2007, Ziegler *et al* 1990). PET detectors are required to have a fast response in order to precisely and accurately identify positron annihilation events that are assumed to have occurred along a virtual tube of response (ToR) connecting the detectors.

Time of flight (ToF) PET is able to reduce the photon emission position uncertainty along the ToR using the flight time difference of the two annihilation photons (Budinger 1983). Compared to conventional PET, the use of ToF information results in faster convergence of the reconstruction or in equivalent noise levels at lower counts and in enhanced lesion detectability in the reconstructed image (Surti *et al* 2006, Surti and Karp 2009). To date, ToF systems with typical time resolutions in the range between 500 and 900 ps are able to provide an increase in the signal to noise ratio (SNR) of the reconstructed image which becomes more significant with increased patient size (Karp *et al* 2008, Moses 2007). As the size of the imaging subject becomes smaller, higher (smaller variance) time resolution compared to the aforementioned values becomes necessary in order to maintain the image SNR. In addition it has been shown that the timing performance of current ToF systems is degraded with increasing count rate and this effect is expected to be larger at higher (smaller values) time resolutions (Surti *et al* 2007). Current efforts from various groups are focusing on exploring the temporal limits of PET detectors and develop designs that provide more accurate energy, time and position information (Kuhn *et al* 2004, Levin 2008, Schaart *et al* 2009, 2010, Daube-Witherspoon *et al* 2010).

Our efforts focus in developing detectors with combined ToF and depth of interaction (DoI) information. Despite the obvious benefit of the combination of ToF and DoI in a PET system, as outlined in figure 1, it will be shown that ToF depends on DoI, and thus proper identification of the latter may increase the accuracy at which the former can be determined. The effect of combined DoI and ToF information on tumor detectability has recently been demonstrated with promising results (Kardmas *et al* 2009). In that study the DoI is modeled in terms of a point spread function (PSF) for every detector pair. However, such a model can only provide a prediction of the DoI probability over the course of a PET acquisition based on the shape of the PSF. We opt for extraction of DoI by means of measurement with appropriate DoI-capable detectors in order to assess its effect on the ToF information on an event-by-event basis. The development of specialized detector designs that are able to provide DoI information is rapidly advancing, resulting in a large variety of DoI-encoding architectures and algorithms (Du *et al* 2008, 2009, Ito *et al* 2010, Maas *et al* 2009, Ling *et al* 2008, Yang *et al* 2009).

Although there has been recent work in developing PET detectors with DoI and ToF capabilities (Bauer *et al* 2010, Kim *et al* 2010, Shibuya *et al* 2008), the effect of DoI in ToF has not been extensively studied due to the fact that the time resolution values of typical PET detectors (a few nanoseconds) are not low enough in order for the DoI to have a considerable effect (tens to hundreds of picoseconds). In addition, extraction of DoI information is typically considered in pre-clinical PET system design only because the parallax positioning error

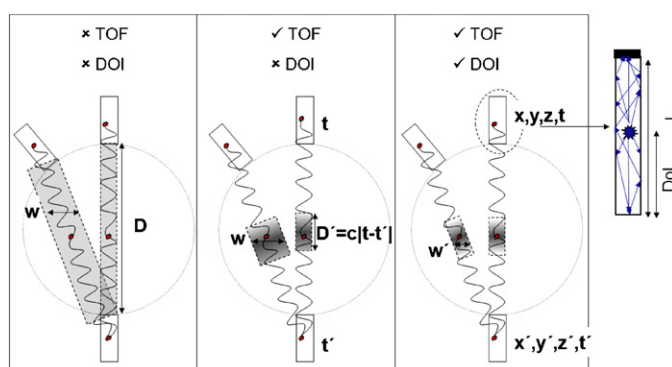


**Figure 1.** From left to right: detector elements without photon DoI or ToF capabilities cannot accurately localize the annihilation events along a ToR between two detector elements (left). ToF information makes this localization more precise by confining it in a ToF kernel (middle). Based on DoI the ToR width becomes narrower, for oblique lines offset from the center (right). In addition, as described in this paper, DoI information is correlated with ToF information and may potentially be exploited to more accurately determine the position and width of the applied ToF kernel.

associated with varying DoI (figure 1) is more prominent in small field of views (FoVs), while ToF information has, so far, a considerable effect only for imaging subjects of a much larger size. However, the development of PET imaging systems dedicated to specific organs, such as the breast or the brain, necessitate the extraction of DoI information given the fact that these organs cover a high fraction of the FoV of the imaging system which, in turn, is significantly smaller than the FoV of whole body imaging systems (Heiss *et al* 2004, Zhang *et al* 2007).

The purpose of this study is to investigate the combined effects of scintillation crystal attributes and DoI on the time resolution degradation of PET detectors in order to determine the optimum attributes for a PET detector design that will minimize these effects. We opt in properly identifying and isolating these effects from any further influence from the photodetector. We thus perform a combined analytical and Monte Carlo (MC) modeling of the optical processes occurring in the scintillator volume without modeling the effect of the photodetector, which is a subject of a separate study.

## 2. Materials and methods

For this study the scintillator of choice is lutetium (yttrium) oxyorthosilicate (LSO or LYSO: Suzuki *et al* 1993, Ludziejewski *et al* 1995, Naud *et al* 1996) read out by silicon photomultipliers (SiPMs: Renker 2006, Renker and Lorenz 2009, Spanoudaki and Levin 2010); however, the general methodology and implications apply to other scintillation materials and photodetectors. L(Y)SO crystals have well-studied properties in terms of light output and decay time; however, the different crystal dimensions as well as surface treatments may affect significantly the response time properties of scintillation detection. We compare the effects of these crystal attributes, namely crystal surface finish and crystal length, as well as the effect of DoI of the annihilation quanta on light yield and time response in both simulation and experiment.

### 2.1. Physical parameter modeling

**2.1.1. Analytical derivations.** The occurrence of a scintillation event in time depends upon: (1) the 511 keV photon flight time from the origin of the annihilation event to the edge of the

FoV of the scanner ( $t_{\text{flight}}$ ), (2) the combination of the flight time of the annihilation photon from the edge of the crystal to the interaction point and the flight time of the generated *unscattered* optical photons within the crystal volume from the interaction point to the photodetector ( $t_{\text{DoI}}$ ), (3) the optical transit time (henceforth referred to as OTT) of the generated *scattered* optical photons within the crystal volume ( $t_{\text{OTT}}$ ) and (4) the charge transit time (henceforth referred to as CTT) in the photodetector ( $t_{\text{CTT}}$ ). The actual time of occurrence of the scintillation event will thus be the sum of the above four variables:

$$t_{\text{event}} = t_{\text{flight}} + t_{\text{DoI}} + t_{\text{OTT}} + t_{\text{CTT}} \quad (1)$$

with a probability density function (pdf) given as follows:

$$\text{pdf}(t_{\text{event}}) = \begin{cases} \text{pdf}(t_{\text{flight}}) \otimes \text{pdf}(t_{\text{DoI}}) \otimes \text{pdf}(t_{\text{OTT}}) \otimes \text{pdf}(t_{\text{CTT}}) & \text{OTT} \neq f(\text{DoI}) \\ \text{pdf}(t_{\text{flight}}) \otimes \text{pdf}(t_{\text{DoI}}, t_{\text{OTT}}) \otimes \text{pdf}(t_{\text{CTT}}) & \text{OTT} = f(\text{DoI}) \end{cases} \quad (2)$$

The desired ToF information is  $t_{\text{flight}}$  degraded by  $t_{\text{DoI}}$ ,  $t_{\text{OTT}}$  and  $t_{\text{CTT}}$ , and their associated variances, as shown in figure 2. Additional factors affecting the time information, such as quantum mechanical limits in the emission of the two annihilation photons (Irby 2003, Gauthier and Hawton 2010) are part of a separate investigation.

The ToF difference of the two annihilation photons  $\Delta t$  which is used to extract position information  $\Delta x$  for event localization along a ToR is directly proportional to  $\Delta x$  when the scintillation photons are produced at the same depth in both crystals and do not encounter scatter at the crystal interfaces prior to detection (figure 2, top):

$$\Delta t = t_2 - t_1 = \frac{2\Delta x}{c} = \Delta t_{\text{flight}}, \quad (3)$$

where  $t_1$ ,  $t_2$  are the detection times of the two annihilation events from each scintillation detector. If different interaction depths within each crystal are assumed then (figure 2, center)

$$\Delta t = t_2 - t_1 = \Delta t_{\text{flight}} + (\text{DoI}_2 - \text{DoI}_1) \cdot \frac{1-n}{c} = \Delta t_{\text{flight}} + \Delta t_{\text{DoI}}, \quad (4)$$

where  $\text{DoI}_1$ ,  $\text{DoI}_2$  are the interaction depths of the annihilation photons at each scintillator and  $n$  is the refractive index of the scintillation material ( $n = 1.82$  for LYSO). In the following, the part of  $\Delta t_{\text{DoI}}$  attributed solely to optical photons will be studied owing the larger refractive index of the scintillation crystal for visible wavelengths. If optical photon scatter within the confined crystal volume is also considered the time information is further distorted (figure 2, bottom):

$$\Delta t = t_2 - t_1 = \Delta t_{\text{flight}} + \Delta t_{\text{DoI}} + \Delta t_{\text{OTT}}, \quad (5)$$

where  $\Delta t_{\text{OTT}}$  is a time delay difference proportional to the number of surfaces encountered by the scattered optical photons prior to their detection.

The contribution of the terms  $\Delta t_{\text{DoI}}$  and  $\Delta t_{\text{OTT}}$  to the extraction of ToF information depends on the decay profile and physical properties of the scintillation crystal. For an ideal crystal with instantaneous scintillation the first detected scintillation photons (from which time information is extracted) encounter minimal scatter or no scatter at all within the crystal volume (depending on the crystal surface treatment) and  $\Delta t_{\text{OTT}}$  is negligible compared to  $\Delta t_{\text{DoI}}$ . The latter correlates in a linear way with DoI, according to equation (4). For a more

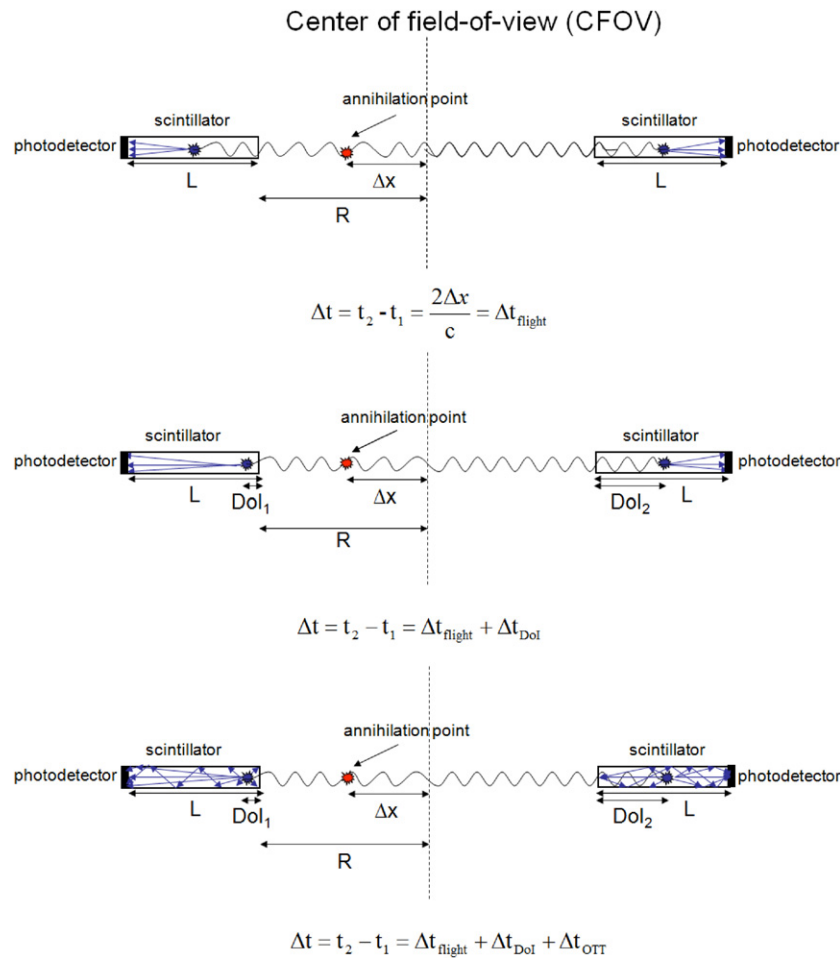


**Figure 2.** Illustration of the different blurring factors that affect the relationship of the ToF information  $\Delta t$  with the position information  $\Delta x$ . Top: the annihilation photons interact at the same depth in both crystals and the detected scintillation photons are not reflected at the crystal faces. Center: the difference in DoI at each crystal will result in an additive factor to the arrival time. Bottom: an additional blurring term is introduced due to the increased light photon flight path variance from their multiple reflections at the crystal faces prior to detection.

realistic crystal with a finite scintillation decay profile, it will be shown that the first detected scintillation photons have encountered scatter prior to detection thus  $\Delta t_{\text{OTT}}$  is dominant over  $\Delta t_{\text{DoI}}$ . In addition  $\Delta t_{\text{OTT}}$  correlates with DoI depending on the crystal surface treatment.

**2.1.2. Optical simulation: photon transport within the crystal volume.** For modeling the scintillation light transport the simulation package DETECT2000 was used (Moisan *et al* 2000). DETECT2000 is a C++ based MC platform developed to simulate the generation of scintillation photons within the crystal volume and predict their detection, transmission or absorption based on pre-defined optical properties of scintillators. For this study the following attributes are modeled:

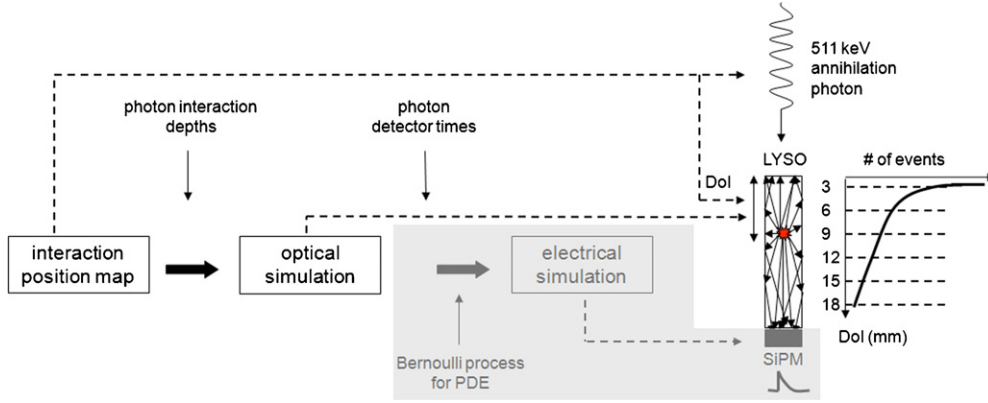


**Figure 3.** Block diagram of the complete simulation process of a LYSO–SiPM detector element. The DoI is modeled either as discrete equidistant points within the crystal volume (dashed lines on the far right diagram) or as points following the exponential attenuation law of radiation (solid curve on the same diagram).

- Position of scintillation light generation: based on literature results for the light output of LYSO the transport of a given number of generated optical photons is simulated either at various positions within the crystal volume according to the 511 keV attenuation profile in LYSO ( $\mu = 0.87 \text{ cm}^{-1}$ ), or at a predefined constant location (figure 3). The 511 keV attenuation profile in LYSO is calculated analytically based on the exponential law of radiation with initial intensity  $I_0$  traversing a material of thickness  $x$ :

$$I(x) = I_0 \cdot e^{-\mu \cdot x}, \quad (6)$$

where  $I$  is the non-attenuated radiation intensity and  $\mu$  is the linear attenuation coefficient for a given absorbing material and at a given energy of the radiation quanta. The total attenuated radiation intensity  $I'$  as a function of the attenuating medium thickness is thus given by

$$I(x)' = I_0 - I = I_0 \cdot (1 - e^{-\mu \cdot x}). \quad (7)$$

The quantity  $I'$  is indicative of the cumulative distribution function (cdf) describing the total attenuation per absorber thickness. The attenuation per unit length is then extracted from the first derivative of the above defined cdf and is indicative of the pdf of radiation absorption as a function of interaction depth:

$$I''(x) = \frac{dI'(x)}{dx} = I_0 \cdot \mu \cdot e^{-\mu \cdot x}. \quad (8)$$

For statistical significance 1000 interaction depths ( $I_0 = 1000$ ) are randomly generated according to a uniform distribution  $P(x)$ ,

$$P(x) dx = \begin{cases} \frac{dx}{\text{crystal length}} & 0 \leq x \leq \text{crystal length} \\ 0 & \text{elsewhere,} \end{cases} \quad (9)$$

and subsequently transformed to the desired distribution  $I''(y)$  through the requirement (Press *et al* 1992):

$$|P(y) dy| = |P(x) dx|, \quad P(y) = I''(y). \quad (10)$$

**Table 1.** The various simulation parameters used in the optical model.

Decay (ns)	Surface finish	Crystal length (mm)	Light output (no. photons)	DoI (mm)
0	polish	5–20	1750–14 000	Attenuation law
0.5 (rise)/40 (decay)	as cut			3–18 (3 mm steps)

- Scintillation crystal size: crystal elements with  $3 \times 3 \text{ mm}^2$  pixel size and three different lengths of 5, 10 and 20 mm are assumed. The pixel size was selected to have a constant value of  $3 \times 3 \text{ mm}^2$  in order to match the SiPM pixel sizes used in DoI–ToF detectors currently under development in our group (section 2.2), thus facilitating accurate comparison between simulation and experiments.
- Scintillation light decay profile: the scintillation light decay is modeled to be instantaneous (ideal case) as well as following a bi-exponential model with a rise time ( $\tau_{\text{rise}}$ ) of 0.5 ns and a decay time ( $\tau_{\text{decay}}$ ) of 40 ns according to the following pdf selected among various suggested models in bibliography (realistic case: Glodo *et al* 2005, Shao 2007):

$$f(t) = \frac{1}{\tau_{\text{decay}} - \tau_{\text{rise}}} \cdot \left( e^{-\frac{t}{\tau_{\text{decay}}}} - e^{-\frac{t}{\tau_{\text{rise}}}} \right). \quad (11)$$

- Scintillation crystal surface treatment: two different crystal surface finishes are assumed, polished and rough (‘as cut’) as defined in (Moisan *et al* 2000). The surfaces are configured to be in contact with a diffuse material chosen to match the refractive index of teflon tape. In this configuration, the simulation assumes specular reflection at the crystal sides in the case of polished surfaces and diffuse (Lambertian) reflection in the case of ‘as cut’ surfaces. It should be pointed out that the ‘as cut’ surface finish is modeled as a generic rough surface with no special definition of the degree of roughness. Even though such definition is possible in DETECT2000 as well as other MC software (van der Laan *et al* 2010), it is difficult to assess how closely it resembles the actual surface roughness of the crystals used in measurement (section 2.2).

Table 1 summarizes the crystal parameters which are varied in each simulation. Even though the crystal material under study is LYSO, different light yields have been modeled in order to take into account systematic losses in the amount of light that is actually producing a signal in the photodetector, such as losses due to the limited photon detection efficiency (PDE) of the latter or losses due to inadequate crystal optical isolation and coupling that could occur during detector preparation. Following the aforementioned rationale, we will conventionally refer to the optical photons that manage to reach the photodetector surface as generated photoelectrons (denoted in figures as ‘phe’).

The focus of this study is to isolate and investigate the effects of DoI and OTT in time resolution; thus, in the following any additional contributions from the scintillator intrinsic energy resolution and the detector electronic noise or CTT will be ignored. In each simulation the value of a certain parameter in table 1 is varied, while all the other parameters are assigned fixed values, resulting in a total of 336 000 optical simulations (the product of all the possible values of the parameters in table 1) realized over a period of several months.

Each simulation is performed for a given time span, typically 500 ns, and the path of each one of the generated photons is tracked until the photon is either detected by the photodetector, absorbed at the crystal surfaces, transmitted through the crystal surfaces or internally trapped in the bulk of the crystal. The simulation provides information about the total number and variance of detected scintillation photons, their flight path and flight time from generation to

detection. In order for the results to have statistical significance, each simulation is repeated 1000 times, each with a different seed for the random number generator required to model all random processes in the simulation.

Using a dedicated processing algorithm, the detected photon events, namely the events that managed to escape the crystal volume and reach the photodetector window, henceforth referred to as photoelectrons, are sorted in time and histograms of the arrival times of the first and the fifth photoelectron are plotted. These histograms will be indicative of  $\text{pdf}(t_{\text{flight}})$  at an arbitrary annihilation point (equation (2)), which convolves either with  $\text{pdf}(t_{\text{DoI}})$  (in the case of instantaneous scintillation) or  $\text{pdf}(t_{\text{OTT}})$  (in the case of an exponentially decaying scintillation profile). The two different photoelectron levels were chosen in such a way that an ideal situation, where the very first photoelectron can actually be probed, is compared with a more realistic situation, where the probing threshold is set above the dark noise level of the SiPM. For the SiPM used in the experiment (section 2.2) the dark count rate at a probing threshold of 2.5 times the single photoelectron pulse height is in the range of a few kHz; therefore, a threshold twice as high (trigger level on the fifth photoelectron) was chosen as a realistic representation of actual noise considerations on timing estimation.

The complete simulation process is summarized in the block diagram of figure 3. The highlighted part in gray illustrates the modeling process of the photodetector which is a subject of a separate study (Spanoudaki and Levin 2011).

## 2.2. Experimental evaluation

The simulated performance is compared with experimentally derived values of coincidence time resolution as a function of crystal element length, surface treatment and DoI. The crystal element used is LYSO of  $3 \times 3 \text{ mm}^2$  cross-sectional area and varying lengths of 5, 10 and 20 mm. The crystal pixel size of  $3 \times 3 \text{ mm}^2$  is selected in order to facilitate individual readout of the scintillation light from commercially available SiPM pixels with typical sizes of either  $3 \times 3 \text{ mm}^2$  or  $1 \times 1 \text{ mm}^2$ , the latter being most appropriate for preclinical imaging. The surface finish of all crystal sides for the experiments is either polished or ‘as cut’. The scintillation light was read out by  $3 \times 3 \text{ mm}^2$  SiPM pixels (Hamamatsu MPPCs, S10362-33-050C,  $50 \mu\text{m}$  microcell size).

For the time resolution measurements a  $^{22}\text{Na}$  point like source was placed between two such detectors and coincidences were registered. The detector signals are fully digitized by a digital storage oscilloscope (Agilent Infiniium DSO90425) at an analog bandwidth of 2.5 GHz and a sampling rate of  $20 \text{ GSamples s}^{-1}$ . The time of each event is estimated from a limited number of digitized samples at the early stages of the signal’s rise, using a lower threshold just above the noise level. Linear fits are applied to both the acquired samples at the noise baseline and at the signal rise and the time stamp is extracted at the point of the intersection of the two fits. Prior to digitization, the detector signals are amplified by a high bandwidth amplifier (Mini-Circuits ZX60-4016E+).

For the measurements of the effects of DoI on time resolution a  $3 \times 3 \times 20 \text{ mm}^3$  crystal of either polished or ‘as cut’ surfaces is irradiated at different points along its length. Electronic collimation of the source is achieved by registering coincidences with a  $3 \times 3 \times 5 \text{ mm}^3$  LYSO crystal coupled to a SiPM, oriented in such a way that its long dimension (5 mm) is aligned orthogonal with respect to the long dimension of the  $3 \times 3 \times 20 \text{ mm}^3$  crystal element (20 mm). In this way the DoI uncertainty along the 20 mm long crystal is roughly 3 mm or less. The different experimental setups are shown in figure 4.

It should be noted that in the methodology followed in this study, the simulated data for an ideal crystal with instantaneous decay are compared to theoretical calculations, while the

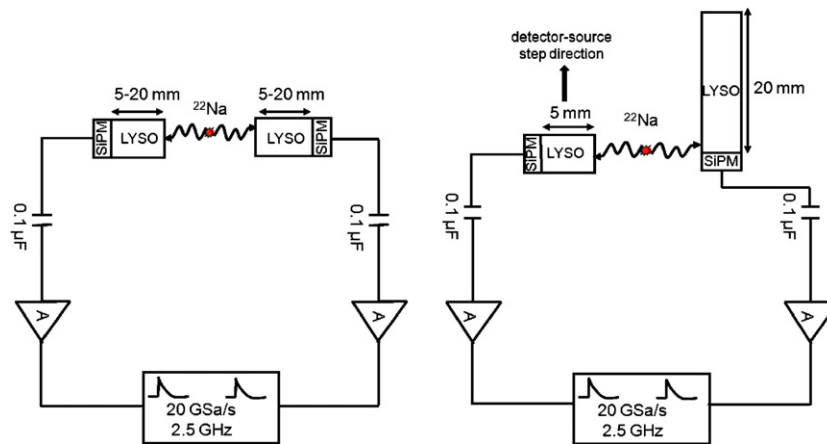


**Figure 4.** The basic experimental setup for time coincidence measurements. Left: measurement of coincidence time resolution as a function of crystal element length and crystal surface treatment. The detectors are irradiated at the top of the crystal ('end-on') with annihilation photons from a  $^{22}\text{Na}$  source. Right: measurement of coincidence time resolution as a function of DoI and crystal surface treatment. The detector of interest (20 mm length) is irradiated from the side at different positions along its length. The two detectors are separated by approximately 1 cm with the point source placed in the middle in the left setup and a few mm closer to the reference detector in the right setup.

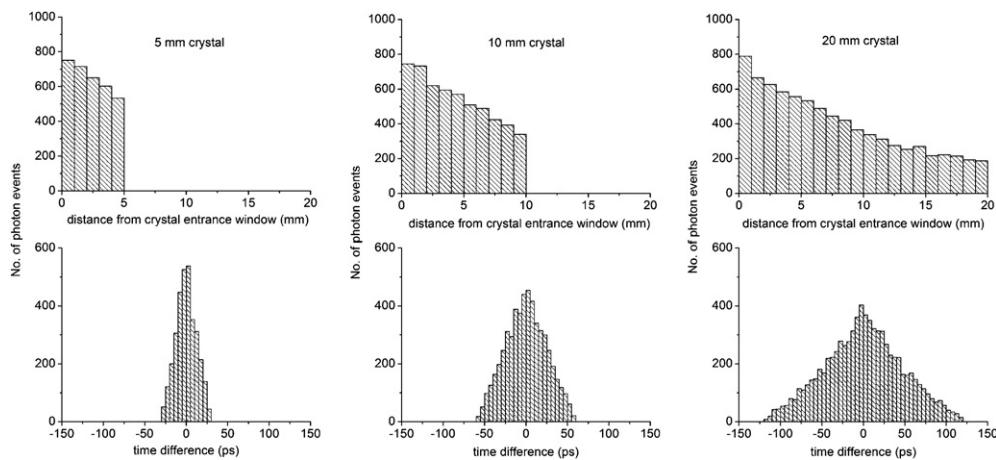


**Figure 5.** Top: analytical calculation of attenuation histograms of annihilation photons in LYSO. Bottom: estimated time coincidence histograms for two crystals with similar attenuation profiles. The crystals are assumed to have the 'end-on' orientation shown in figure 4 (left). Calculations for 5 (left), 10 (center) and 20 mm (right) length crystals are shown.

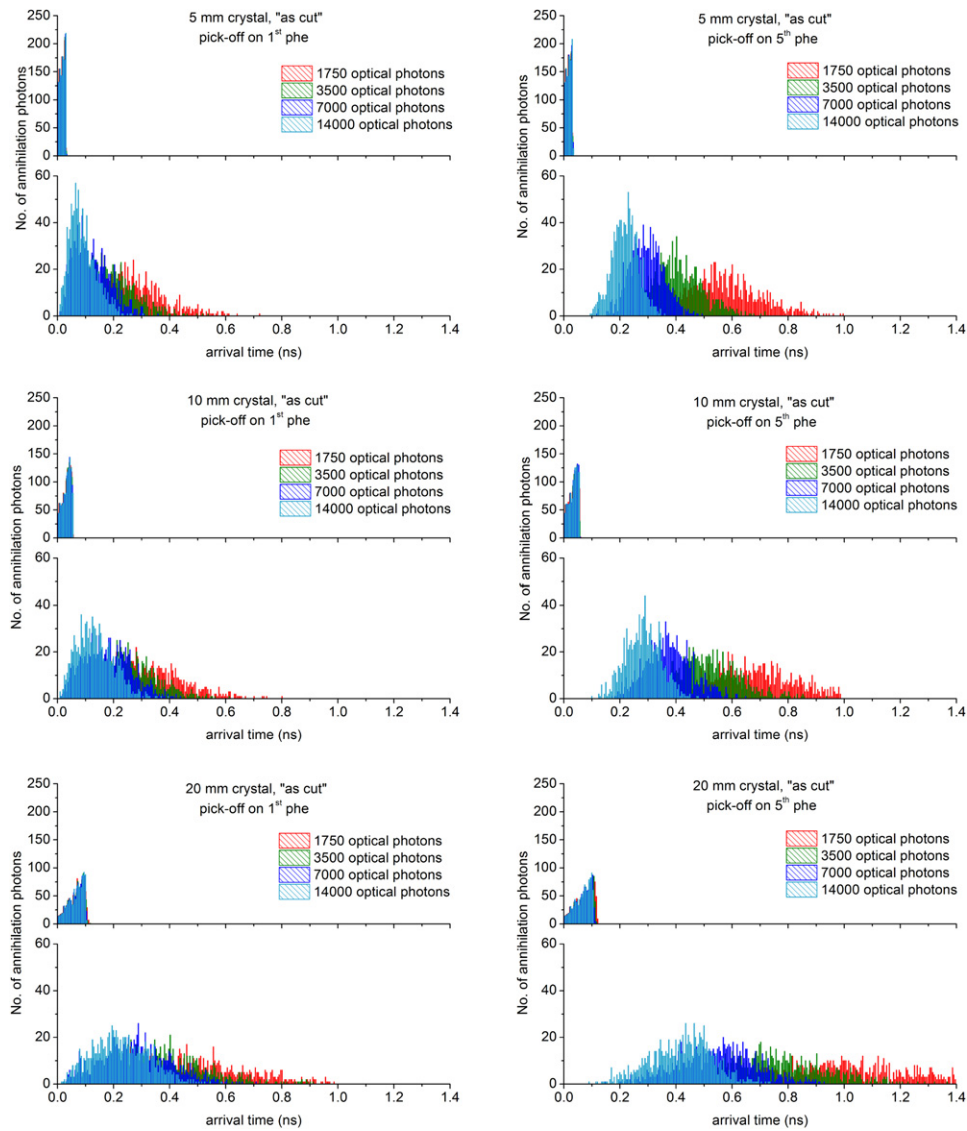


**Figure 6.** Simulated histograms of the arrival time of the first (left) or fifth (right) photoelectron for variable scintillation crystal light yield and for a crystal with rough ('as cut') surfaces ( $3 \times 3 \text{ mm}^2$  pixel cross-section and 5, 10 or 20 mm length). For each crystal length the top histogram is for instantaneous scintillation decay and the bottom histogram is for a scintillation profile with 0.5 ns rise and 40 ns decay.

simulated data for a realistic scintillator following the bi-exponential decay are compared to experimental data.

### 3. Results

#### 3.1. Analytical derivations and physical parameter modeling

Figure 5 illustrates attenuation histograms of approximately 1000 annihilation photons along the length of 5, 10 and 20 mm thick crystal elements, derived using the methodology described

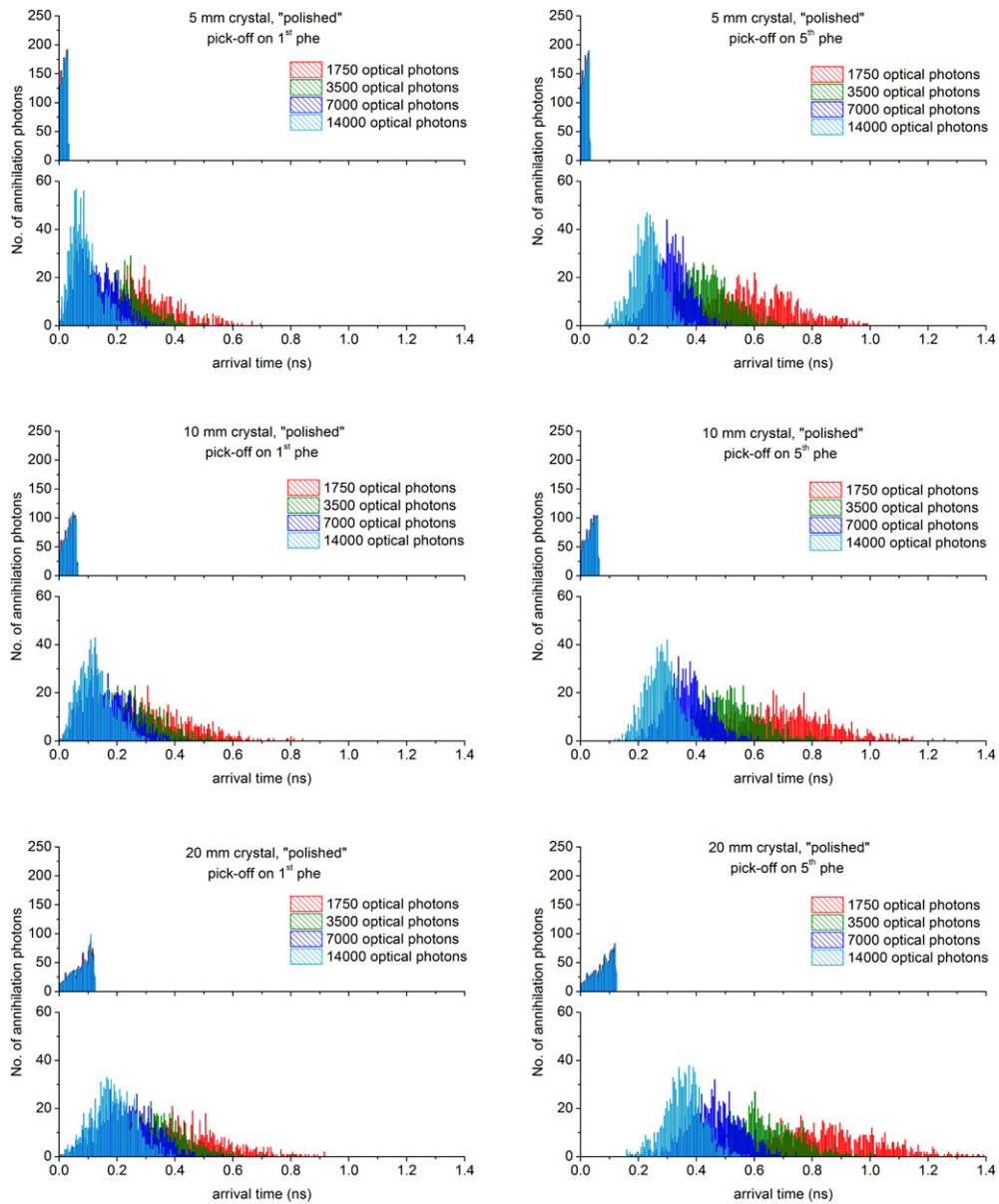
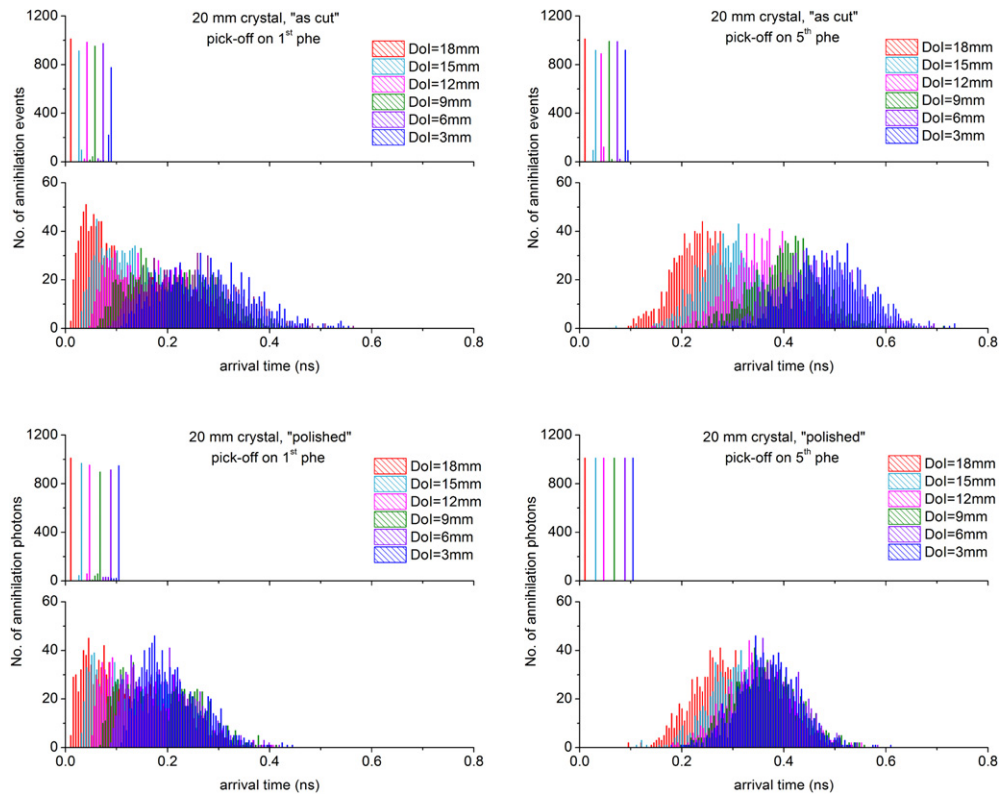


Figure 7. Same description as in figure 6 for a crystal with polished surfaces.

by equations (6)–(10). In the same figure, hypothetical time difference histograms between two crystals with those corresponding attenuation profiles are shown in order to predict the effect of the non-constant DoI on resulting time resolution. In order to simplify calculations, the results refer to 1D attenuation along the crystal length.

Figure 6 shows simulated arrival time (time elapsed from generation of optical photons until detection by the photodetector) histograms for the first and fifth photoelectron created by the photodetector (assuming 100% QE and zero variance of CTT), for ‘as cut’ crystals of different lengths and different scintillator light yields. Figure 7 shows the same results



**Figure 8.** Simulated histograms of the arrival time of the first (left) or the fifth (right) photoelectron at different interaction depths along  $3 \times 3 \times 20 \text{ mm}^3$  crystal with rough ('as cut', top) or polished (bottom) surfaces. For each crystal surface finish condition the top histogram is for instantaneous scintillation decay and the bottom histogram is for a scintillation profile with 0.5 ns rise and 40 ns decay.

for polished crystals. From the row of graphs corresponding to the same crystal length, the top histograms are for a scintillator with ideal temporal response, namely the optical photons generated instantaneously within the crystal volume. The bottom histograms are for a scintillator with a realistic temporal response according to the pdf shown in equation (11). The left column of graphs corresponds to estimation of the arrival time based on the first detected photoelectron, whereas for the right column of graphs the arrival time estimation is based on the fifth detected photoelectron. The irradiation is assumed to be from the entrance window of the crystal (opposite to the photodetector entrance window) and the interaction depths of each of the 1000 511 keV photons simulated follow the exponential attenuation law.

Figure 8 shows arrival time histograms for the first and fifth photoelectron created by the photodetector, for a  $3 \times 3 \times 20 \text{ mm}^3$  crystal of either rough ('as cut') or polished surfaces irradiated at different DoIs. Both ideal and realistic scintillator temporal responses are considered. A light yield of 14 000 optical photons is assumed.

The left graph of figure 9 compares the theoretically derived time resolutions based on the calculated FWHM of the histograms of figure 5 (bottom row) with the derived time resolutions based on the graphs of figures 6 and 7 for the case of a scintillator with instantaneous decay

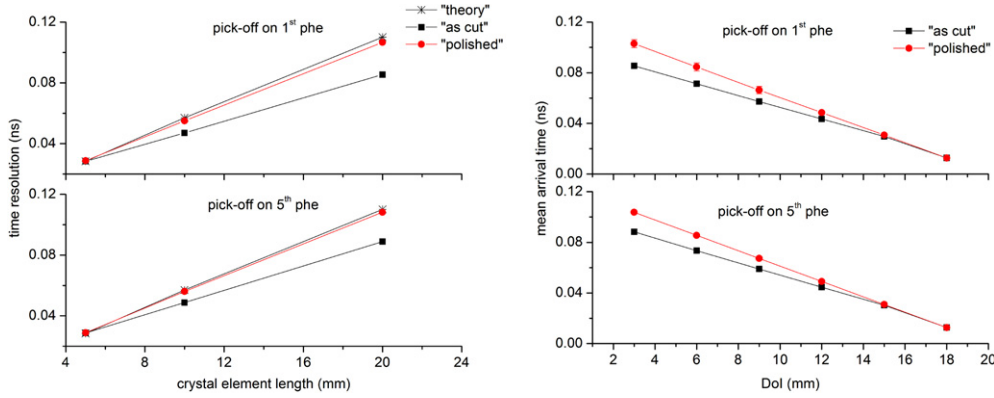


**Figure 9.** Simulated coincidence time resolution (left) and mean arrival time (right) as a function of crystal element length and DoI, respectively, for a crystal with instantaneous scintillation decay and with either ‘as cut’ or polished surfaces. Time pick-off is performed on the first (top row) and the fifth (bottom row) photoelectron. The simulated coincidence time resolution values (left graph) are also compared with the derived FWHM values of the time difference distributions shown on the bottom graphs of figure 5 (denoted as ‘theory’).

**Table 2.** Calculated values of the LYSO refractive index based on the plots of figure 9 (right).

Crystal surface	Refractive index	
	First phe	Fifth phe
rough (‘as cut’)	$1.56 \pm 0.05$	$1.56 \pm 0.04$
polished	$1.806 \pm 0.004$	$1.800 \pm 0.004$

(top rows for each crystal length). For the latter case the FWHM values were calculated based on the following formula:

$$\text{FWHM} = 2.35 * 1.4 * \text{sd}_{\text{single detector}}, \quad (12)$$

where  $\text{sd}_{\text{single detector}}$  is the standard deviation on arrival time as calculated from the histograms of figures 6 and 7 for the case of a scintillator with instantaneous decay (top rows for each crystal length). These histograms refer to single detectors; thus, calculation for a pair of identical detectors (resulting in the multiplication factor of 1.4 in equation (12)) is performed assuming Gaussian distribution of the resulting time difference histogram (resulting in the multiplication factor of 2.35 in equation (12)). The right graph of figure 9 shows the calculated mean arrival time (as extracted from the centroids of the histograms of figure 8 for an ideal scintillator) as a function of DoI. The calculated slopes from applied linear fits on the data of this graph are theoretically proportional to the refractive index of the assumed scintillator (LYSO) according to the formula

$$\text{slope} = \frac{n}{c} \quad (13)$$

as can be derived from equation (4) assuming a single detector element and neglecting the flight time of the annihilation photons within the crystal volume (from the crystal entrance window until the point of interaction). Table 2 shows the calculated values of the LYSO refractive index ( $n = 1.82$ ) for the two different crystal surfaces.

The light output, defined as the number of optical photons detected by the assumed photodetector, and standard deviation of the arrival time, based on the histograms of figures 6

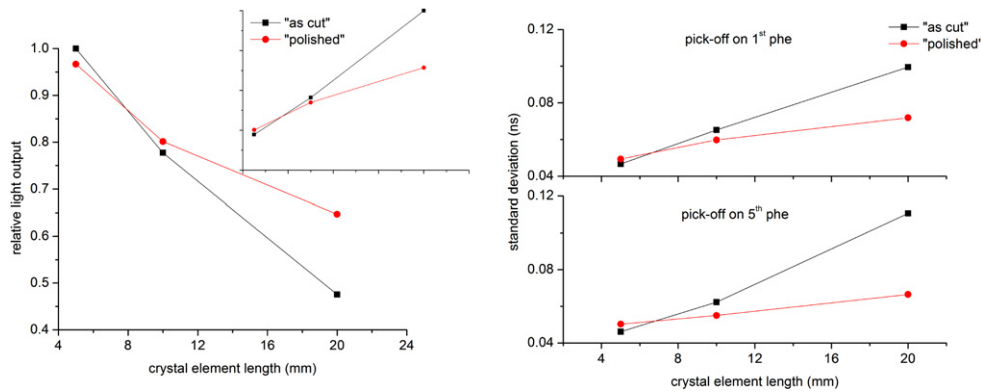


**Figure 10.** Simulated relative light output normalized to the maximum (left) and standard deviation on photon arrival time (right), as estimated from the histograms of figures 6 and 7, as a function of crystal length for time pick-off on the first and fifth photoelectron and for a realistic scintillator decay (40 ns). The inset on the left graph is a plot of  $\frac{1}{\sqrt{\text{light output}}}$  (y-axis of inset) as a function of crystal length (x-axis of inset) thus indicating the portion of dependence of arrival time deviation on crystal length that is attributed to the number of detected optical photons.

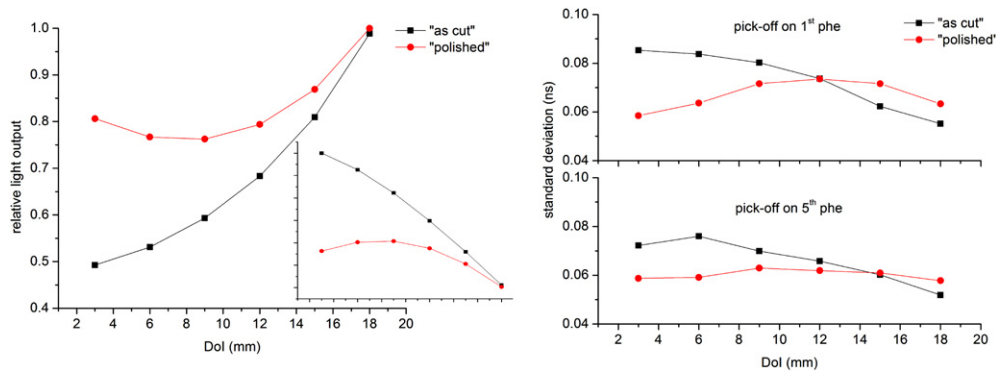


**Figure 11.** Simulated relative light output normalized to the maximum (left) and standard deviation (right) of the arrival time histograms of figure 8, as a function of DoI for time pick-off on the first and fifth photoelectron and for a realistic scintillator decay (40 ns). The inset on the left graph is a plot of  $\frac{1}{\sqrt{\text{light output}}}$  (y-axis of inset) as a function of DoI (x-axis of inset) thus indicating the portion of dependence of arrival time deviation on DoI that is attributed to the number of detected optical photons.

and 7, as a function of crystal element length are shown on the graphs of figure 10 for a realistic scintillator decay profile. A scintillator light yield of 14 000 optical photons is assumed. The light output and standard deviation of the arrival time, based on the histograms of figure 8, as a function of DoI for a crystal length of 20 mm, a light yield of 14 000 and a realistic scintillation decay profile are shown in figure 11. The insets in the left graphs of figures 10 and 11 are indicative of the  $\frac{1}{\sqrt{\text{light output}}}$  dependence on crystal length and DoI, respectively. These plots are to be compared with the dependence of arrival time standard deviation on the same attributes (right graphs of figures 10 and 11), as predicted from the  $\frac{1}{\sqrt{\text{light output}}}$  dependence of time resolution (Paulus 1982, Bell 1966). Although this dependence is not included as a separate additive factor in equations (4) and (5), its contribution is largely reflected in the  $t_{\text{DoI}}$

**Table 3.** Summary of simulation results on the dependence of light output and arrival time standard deviation on crystal length for polished over ‘as cut’ crystals. % values are calculated according to equation (14).

Crystal length (mm)	Light output No threshold (%)	Arrival time standard deviation	
		First phe (%)	Fifth phe (%)
5	3	−6	−9
10	−3	8	12
20	−36	28	40

**Table 4.** Summary of simulation results on the dependence of light output and arrival time standard deviation on DoI for polished over ‘as cut’ crystals. % values are calculated according to equation (14).

DoI (mm)	Light output No threshold (%)	Arrival time standard deviation	
		First phe (%)	Fifth phe (%)
3	−64	31	19
6	−44	24	22
9	−28	11	10
12	−16	0	6
15	−7	−15	−1
18	−1	−15	−11

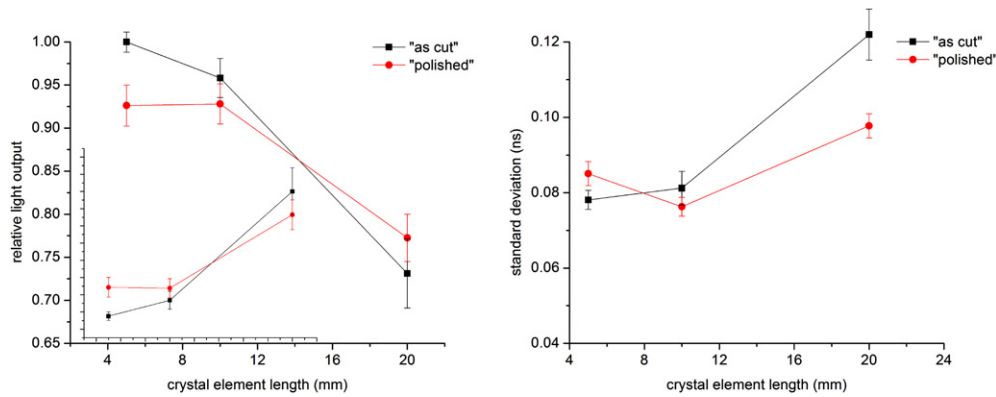


**Figure 12.** Measured relative light output (left) and standard deviation of the arrival time calculated from equation (15) (right) as a function of crystal length for polished and ‘as cut’ crystal surface treatments. A description of the inset on the left graph is provided in the caption of figure 10.

and  $t_{\text{OTT}}$  components due to the underlying Poisson statistics dominating any time pick-off method.

A summary of the simulation results is given in tables 3 and 4. The % values are used to highlight the differences in light output or arrival time between the two different crystal surfaces and are calculated according to the formula

$$\% \text{ value} = 100 \cdot \frac{\text{value}_{\text{'as cut'}} - \text{value}_{\text{polished}}}{\text{value}_{\text{'as cut'}}} \quad (14)$$

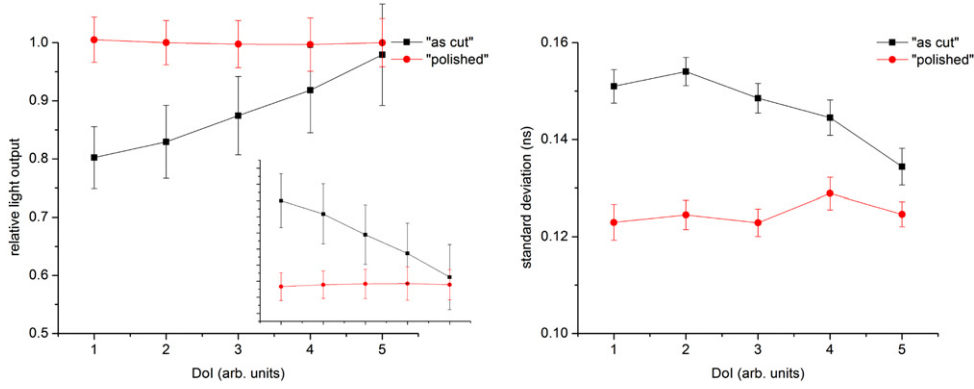


**Figure 13.** Measured relative light output (left) and standard deviation of the arrival time calculated from equation (16) (right) as a function of DoI along a  $3 \times 3 \times 20 \text{ mm}^3$  crystal versus a  $3 \times 3 \times 5 \text{ mm}^3$  crystal element. Data points are separated by 3 mm. A description of the inset on the left graph is provided in the caption of figure 11.

### 3.2. Experimental evaluation

Figure 12 shows light output and timing measurements performed with the setup shown in figure 4 (left) as a function of crystal length for different crystal surface treatments. Only annihilation events with full energy deposition in the crystal have been selected; thus, the lower energy threshold (LET) was set above the Compton edge in order to include only photoelectric events. All the measurements were performed at a bias voltage of 71.9 V for the SiPMs, which was found to be optimum in terms of time performance without leading to SiPM nonlinear response (Spanoudaki and Levin 2010).

Figure 13 shows light output and timing measurements performed with the setup shown in figure 4 (right) as a function of DoI for different crystal surface treatments. For direct comparison with the simulated data, in both figures 12 and 13 (right graph) the calculated FWHM values of the coincidence time resolution were converted to standard deviation values of single detector elements according to the formula

$$\text{sd}_{\text{measurement}_1} = \frac{\text{FWHM}}{2.35 \cdot 1.4} \quad (15)$$

$$\text{sd}_{\text{measurement}_2} = \sqrt{\left(\frac{\text{FWHM}}{2.35}\right)^2 - (\text{sd}_{5 \text{ mm}})^2} \quad (16)$$

for the setups in figure 4 (left) and (right), respectively. Even though there were practical difficulties in reproducing the exact DoI values as in simulation due to mechanical limitations, the various DoI points in the experiment were separated by 3 mm, similar to the simulated DoI points. A summary of the experimental results is given in tables 5 and 6. The % values are calculated according to equation (14).

## 4. Discussion

### 4.1. Simulation results

For the case of instantaneous scintillation decay (ideal case), the arrival time histograms of figures 6 and 7 suggest no dependence on the scintillator light yield, as expected due to the zero

**Table 5.** Summary of experimental results on the dependence of light output and arrival time standard deviation on crystal length for polished over ‘as cut’ crystals. % values are calculated according to equation (14).

Crystal length (mm)	Light output (%)	Arrival time standard deviation (%)
5	7	−9
10	3	6
20	−6	20

**Table 6.** Summary of experimental results on the dependence of light output and arrival time standard deviation on DoI for polished over ‘as cut’ crystals. % values are calculated according to equation (14).

DoI (arb. units)	Light output (%)	Arrival time standard deviation (%)
1	−25	18
2	−20	19
3	−14	17
4	−8	11
5	−2	7

time dispersion of the emitted amount of scintillation light. However there is a dependence on the crystal element length which is directly related to the varying mean distance of the scintillation light origin from the photodetector due to the exponential attenuation law of the 511 keV photons along the crystal length. This result further verifies that for the case of an ideal scintillator the dominating factor responsible for the deviation between  $\text{pdf}(t_{\text{event}})$  and  $\text{pdf}(t_{\text{flight}})$  is  $\text{pdf}(t_{\text{DoI}})$  (equation (2)). No dependence on the trigger level is observed, as represented by which photoelectron (in this case the first or the fifth) is used to estimate the arrival time. When compared to the analytical predictions (figure 5) a better agreement is evident for polished over ‘as cut’ crystals (left graph of figure 9).

For the same, ideal, case the graphs of figure 8 show linear correlation of the distribution centroids with DoI for both cases of polished and ‘as cut’ crystals. When plotting the centroids versus DoI position (right graphs of figure 9), this correlation can be extracted from the calculated slopes of the plots according to equation (13) and is directly related to the LYSO refractive index. It can be seen from the quantitative data of table 2 that the calculated values of the refractive index are closer to the theoretical value for polished compared to ‘as cut’ crystal surfaces. The deviation in the case of ‘as cut’ crystals is attributed to the presence of a weak OTT contribution (equation (5)) due to scatter of the optical photons in the micro-surfaces of the crystal surface in contact with the photodetector, prior to detection. In either case, however, the derived values verify the assumption that for instantaneous scintillation decay  $\Delta t_{\text{DoI}}$  is the dominant factor of time dispersion.

For the realistic case of scintillation decay (where  $\Delta t_{\text{OTT}}$  is dominant over  $\Delta t_{\text{DoI}}$ ) the arrival time histograms of figures 6 and 7 suggest an obvious dependence of time resolution on crystal element length and crystal element light yield. As the crystal element length decreases and the light yield increases, the standard deviation on the arrival time of the first/fifth photoelectron decreases. The effect of surface treatment on time resolution is, however, not straightforward and demonstrates a dependence on the crystal element length. For small crystal elements a rough (‘as cut’) crystal surface appears to improve time resolution compared to polished surfaces. As the crystal element length increases this trend is reversed resulting in better

achieved time resolution for longer crystals with polished surfaces. A similar observation can be made for the dependence of the light output as a function of crystal length which consequently leads to a good agreement between the dependence of  $\frac{1}{\sqrt{\text{light output}}}$  (inset graph in figure 10, left) and time resolution on crystal length (figure 10, right).

This reversed trend is explained by the fact that the rough surface crystal time response has a somewhat stronger correlation with the DoI, compared to the time response for a crystal with polished surfaces. For short crystal elements with rough surfaces the contribution of DoI to the time response demonstrates only a small standard deviation whereas as the crystal length increases, this deviation cannot be ignored. Figure 11 (right) shows clearly that the arrival time standard deviation appears to have a more monotonically varying pattern with DoI in the case of a rough compared to a polished crystal, which is also predicted by the inverse square law of the detected optical photons (inset graph in figure 11, left).

The effect of the trigger level observed in the right graphs of figures 10 and 11 is reversed depending on the crystal surface treatment especially for a 20 mm long crystal element. In the case of interaction depths following the exponential attenuation law (figure 10) a higher trigger level (fifth photoelectron) minimizes the arrival time standard deviation for polished surfaces, while for rough surfaces the arrival time dispersion is lower for lower trigger level (first photoelectron). In the case of a constant interaction depth (figure 11) there is a consistent improvement (minimization) of the arrival time standard deviation for higher trigger level for both crystal surface treatments.

#### 4.2. Experimental results

Figure 12 shows that the time resolution degrades with increasing crystal length, whereas the dependence of time resolution on crystal surface treatment is more apparent for increasing crystal length, an effect which is also verified by the simulation results (figure 10). The calculated values of standard deviation in the arrival time for small crystal length deviate from the simulated values primarily due to the CTT limits of the photodetector that are not included in the simulation.

The experimental derivation of the DoI dependence of time resolution shown in figure 13 demonstrates the same trend as the simulation data of figure 11, namely a more monotonic dependence of time resolution on DoI for rough over polished crystals. There is an overall shift of the measured arrival time standard deviation values compared to the simulated ones, owing to less efficient light coupling of the detectors, as well as to the source position, placed a few mm closer to the reference detector (figure 4, right) resulting in a non-zero  $\Delta t_{\text{flight}}$ . For detectors with time resolutions not low enough to resolve (at more than a  $\sigma$ ) position differences of a few mm, this difference in  $t_{\text{flight}}$  translates to a broadening of the time standard deviation. The excessive error bars in the left plots of figures 12 and 13 are indicative of the detector energy resolution which is not taken into account in the simulated data.

Tables 3–6 show comparable trends in both measurement and simulation with a noticeable deviation in the case of light output. Since quantitative analysis for the simulation results was performed for a light yield of 14 000 optical photons, the deviation is attributed to reduced light detection efficiency in the experiment. In addition, even though simulation allows to easily probe the arrival of each individual photoelectron, this is not usually the case in experiment where detector noise may degrade the ability of single photoelectron resolution. The threshold set for the timing measurements was low enough in order to trigger on the first few photoelectrons generated from scintillation detection, but high enough in order to avoid triggering on noise. Our current efforts focus on modeling the SiPM pulse formation

**Table 7.** Comparison between simulated and experimentally derived results. % values indicate the variation of experimental and simulated values over the complete range of selected crystal lengths (15 mm) and over a mean 3 mm DoI interval.

	Dependence on crystal length		Dependence on DoI	
	Simulation (%)	Experiment (%)	Simulation	Experiment
Light output	130	190	$\frac{16\%}{3 \text{ mm}}$	$\frac{18\%}{3 \text{ mm}}$
Arrival time standard deviation	540	320	$\frac{26\%}{3 \text{ mm}}$	$\frac{12\%}{3 \text{ mm}}$

triggered by a scintillation event (highlighted region of figure 3, Spanoudaki and Levin 2011) and include the modeled response in the time pick-off algorithm.

The experimental results inevitably encompass both the scintillator and the photodetector effects. However in both simulation and experiment, critical performance parameters, such as light output and time resolution, are studied as a function of the same, crystal specific, attributes allowing thus for comparison of the relative trends observed. The observed trends are in good agreement in both cases and appear to be offset by the photodetector performance (mostly CTT and dark noise) in the case of measurement. Table 7 summarizes the % variation of the experimental and simulated results (tables 3–6) over the complete range of selected crystal lengths (15 mm) and over a mean 3 mm distance between subsequent DoI positions.

## 5. Conclusion

This study aims to provide an understanding of the physical factors which influence the accuracy of temporal information for scintillation events generated in the confined volume of small detector elements. Even though such topic has previously been addressed through several theoretical and experimental studies, in this study we focus our research to meet the demands of modern PET detector technology which evolves toward detector designs that provide enhanced spatial resolution (narrower crystal elements) and enhanced imaging sensitivity (longer crystal elements).

Features such as ToF and DoI are already acknowledged to improve image SNR and spatial resolution, respectively, which naturally leads to the need to study their co-dependence. This need becomes even more evident with improved time resolution which, if further improved (i.e. by means of faster scintillators), will pose the challenge to probe physical effects that were not previously observable due to the limited detector performance. This is illustrated in the examples of an ideal and a realistic scintillator, studied in this paper, where the measured ToF information, represented by  $\Delta t$  in equations (4) and (5), is dependent on different blurring factors. In the case of an ideal scintillator the blurring factor is DoI, namely a measurable quantity, which if properly identified can be exploited to improve the properties of  $\text{pdf}(\Delta t)$ , that determines the ToF kernel. In the case of a realistic scintillator the blurring factor is OTT, a quantity which is not measurable in a direct way but can be indirectly identified through its association with DoI, as the above results suggest. The slow decay time of current scintillators makes this identification a rather difficult task, even for the case of LYSO. However, as the development of scintillation materials with higher photon emission rate progresses, the measurable ToF information will show a more direct correlation with DoI which can be exploited to isolate or even suppress the OTT contribution. An example of such material is  $\text{LaBr}_3$  (van Loef *et al* 2001 and 2002) whose properties better approach those of an ideal scintillator.

Our research currently aims at exploiting the findings of this study to guide the design of future ToF–PET detectors employing pixellated crystal elements. According to the above

results the ideal ToF–PET detector will consist of a scintillator of instantaneous decay with polished surfaces which enables the use of DoI information in order to improve the detector time performance according to equation (4). The existing technology does not allow for such ideal designs mostly due to limitations in the decay time of the scintillation materials being in the order of a few tens of ns. Using existing scintillation crystals, the contribution of OTT distorts the linear dependence of time information on DoI through equation (5), where OTT also depends on DoI. This dependence appears to be stronger for crystals with rough (‘as cut’) surfaces compared to polished. Thus, for ToF–PET detector designs that aim in disentangling the contribution of DoI on timing information, selection of crystals with rough surfaces may be beneficial, depending on the DoI identification scheme used. For DoI designs aiming at extraction of continuous information by employing long crystals, such as dual ended crystal readout, surface treatment is a critical factor that needs to be taken into consideration. For DoI designs employing shorter crystal elements, such as layered detectors, surface treatment may be of less importance, especially given the fact that the DoI information is of discrete and more coarse nature.

The identification of DoI and its association with timing information has further implications in the way that ToF reconstruction is performed. As opposed to the typical, non-ToF reconstruction where the DoI effects have an impact predominantly in oblique ToRs, the implementation of ToF information in the reconstruction algorithm is affected by DoI even for ToRs with non-oblique detector pairs. This is illustrated in figure 1 where the position and the width of the ToF kernel is optimized when both ToF and DoI information are available. In addition, the ToF difference information  $\Delta t$ , as extracted from equation (5), applies to all ToRs regardless of their obliqueness. We are currently performing MC simulations of a full ring DoI–ToF system with variable DoI and timing resolutions and variable FoVs in order to assess their actual effect on quantification and image quality, as well as to investigate methods for implementing the DoI information in the ToF reconstruction algorithm.

## Acknowledgment

This work is supported in part by the AXA Research Fund.

## References

- Bauer F, Aykac M, Eriksson L and Schmand M 2010 Depth of interaction with a 3-dimensional checkerboard arrangement LSO–LSO block *IEEE Trans. Nucl. Sci.* **57** 971–5
- Bell R E 1966 Comparison of leading-edge and crossover timing in coincidence measurements *Nucl. Instrum. Methods Phys. Res. A* **42** 211–2
- Binkley D M 1994 Optimization of scintillation-detector timing systems using Monte Carlo analysis *IEEE Trans. Nucl. Sci.* **41** 386–93
- Budinger T F 1983 Time-of-flight positron emission tomography: status relative to conventional PET *J. Nucl. Med.* **24** 73–8
- Clinthorne N H, Petrick N, Rogers L W and Hero A O 1990 A fundamental limit on timing performance with scintillation detectors *IEEE Trans. Nucl. Sci.* **37** 658–63
- Daube-Witherspoon M E, Surti S, Perkins A, Kyba C C M, Wiener R, Werner M E, Kulp R and Karp J S 2010 The imaging performance of a LaBr<sub>3</sub>-based PET scanner *Phys. Med. Biol.* **55** 45–64
- Du H, Yang Y and Cherry S R 2008 Comparison of four depth-encoding PET detector modules with wavelength shifting (WLS) and optical fiber read-out *Phys. Med. Biol.* **53** 1829–42
- Du H, Yang Y, Glodo J, Wu Y, Shah K and Cherry S R 2009 Continuous depth-of-interaction encoding using phosphor-coated scintillators *Phys. Med. Biol.* **54** 1757–77
- Gauthier I and Hawton M 2010 Photon correlations in positron annihilation *Phys. Rev. A* **81** 062121
- Glodo J, Moses W, Higgins W, van Loef E, Wong P, Derenzo S, Weber M and Shah K 2005 Effects of Ce concentration on scintillation properties of LaBr<sub>3</sub>:Ce *IEEE Trans. Nucl. Sci.* **52** 1805–8

- Heiss W-D, Habedank B, Klein J C, Herholz K, Wienhard K, Lenox M and Nutt R 2004 Metabolic rates in small brain nuclei determined by high-resolution PET *J. Nucl. Med.* **45** 1811–5
- Hero A O, Clinthorne N H and Rogers L W 1991 A lower bound on PET timing estimation with pulse pile-up *IEEE Trans. Nucl. Sci.* **38** 709–12
- Irby V D 2003 Physical limitations on quantum nonlocality in the detection of photons emitted from positron–electron annihilation *Phys. Rev. A* **67** 034102
- Ito M, Lee J S, Park M-J, Sim K-S and Hong S J 2010 Design and simulation of a novel method for determining depth-of-interaction in a PET scintillation crystal array using a single-ended readout by a multi-anode PMT *Phys. Med. Biol.* **55** 3827–41
- Kardmas D J, Casey M E, Conti M, Jakoby B W, Lois C and Townsend D W 2009 Impact of time-of-flight on PET tumor detection *J. Nucl. Med.* **50** 1315–23
- Karp J S, Surti S, Daube-Witherspoon M E and Muehllehner G 2008 Benefit of time-of-flight in PET: experimental and clinical results *J. Nucl. Med.* **49** 462–70
- Kim H, Frisch H, Chen C-T, Genat J-F, Moses W W, Choong W S and Kao C M 2010 A design of a PET detector using micro-channel plate photomultipliers with transmission-line readout *Nucl. Instrum. Methods Phys. Res. A* **622** 628–36
- Kuhn A, Surti S, Karp J S, Raby P S, Shah K S, Perkins A E and Muehllehner G 2004 Design of a lanthanum bromide detector for time-of-flight PET *IEEE Trans. Nucl. Sci.* **51** 2550–7
- Levin C S 2008 New imaging technologies to enhance the molecular sensitivity of positron emission tomography *Proc. IEEE* **96** 439–67
- Ling T, Burnett T H and Miyaoka R S 2008 Parametric positioning of a continuous crystal PET detector with depth of interaction decoding *Phys. Med. Biol.* **53** 1843–63
- Ludziejewski T, Moszynska K, Moszynski M, Wolski D, Klamra W, Norlin L O, Devitsin E and Kozlov V 1995 Advantages and limitations of LSO scintillator in nuclear physics experiments *IEEE Trans. Nucl. Sci.* **42** 328–36
- Maas M C, Schaart D R, van der Laan D J, Bruyndonckx P, Lemaître C, Beekman F J and van Eijk C W E 2009 Monolithic scintillator PET detectors with intrinsic depth-of-interaction correction *Phys. Med. Biol.* **54** 1893–908
- Moisan C, Cayouet F and McDonald G 2000 DETECT2000 *The Object Oriented C++ Language Version of DETECT. A Program for Modeling Optical Properties of Scintillators* Version 5.0
- Moses W W and Ullisch M 2006 Factors influencing timing resolution in a commercial LSO PET camera *IEEE Trans. Nucl. Sci.* **53** 78–85
- Moses W W 2007 Recent advances and future advances in time-of-flight PET *Nucl. Instrum. Methods Phys. Res. A* **580** 919–24
- Moszynski M, Ludziejewski T, Wolski D, Klamra W and Avdeychikov V V 1996 Timing properties of GSO, LSO and other Ce doped scintillators *Nucl. Instrum. Methods Phys. Res. A* **372** 51–8
- Naud J D, Tomborello T A, Melcher C L and Schweitzer J S 1996 The role of cerium sites in the scintillation mechanism of LSO *IEEE Trans. Nucl. Sci.* **43** 1324–8
- Paulus T J 1982 Principles and applications of timing spectroscopy *Application Note AN-42, EG&E*
- Petrick N, Clinthorne N H, Rogers L W and Hero A O 1991 First photoelectron timing error evaluation of a new scintillation detector model *IEEE Trans. Nucl. Sci.* **38** 174–7
- Post R F and Schiff L I 1950 Statistical limitations on the resolving time of a scintillation counter *Phys. Rev.* **80** 1113
- Press W H, Teukolsky S A, Vetterling W T and Flannery B P 1992 *Numerical Recipes in C. The Art of Scientific Computing* (Cambridge: Cambridge University Press)
- Renker D 2006 Geiger-mode avalanche photodiodes, history, properties and problems *Nucl. Instrum. Methods Phys. Res. A* **567** 48–56
- Renker D and Lorenz E 2009 Advances in solid state photon detectors *J. Instrum.* **4** P04004
- Schaart D R, Van Dam H T, Seifert S, Vinke R, Dendooven P, Loehner H and Beekman F J 2009 A novel, SiPM-array-based, monolithic scintillator detector for PET *Phys. Med. Biol.* **54** 3501–12
- Schaart D R, Seifert S, Vinke R, Van Dam H T, Dendooven P, Loehner H and Beekman F J 2010 LaBr<sub>3</sub>:Ce and SiPMs for time of flight PET: achieving 100 ps coincidence resolving time *Phys. Med. Biol.* **55** N179–89
- Shao Y 2007 A new timing model for calculating the intrinsic timing resolution of a scintillator detector *Phys. Med. Biol.* **52** 1103–17
- Shibuya K *et al* 2008 Timing resolution improvement using DOI information in a four-layer scintillation detector for TOF-PET *Nucl. Instrum. Methods Phys. Res. A* **593** 572–7
- Spanoudaki V Ch and Levin C S 2010 Photo-detectors for time of flight positron emission tomography (ToF-PET) *Sensors* **10** 10484–505
- Spanoudaki V Ch and Levin C S 2011 Scintillation induced response in passively-quenched Si-based single photon counting avalanche diode arrays *Opt. Express*. in press

- Surti S and Karp J S 2009 Experimental evaluation of a simple lesion detection task with time-of-flight *Phys. Med. Biol.* **54** 373–84
- Surti S, Karp J S, Popescu L M, Daube-Witherspoon M E and Werner M 2006 Investigation of time-of-flight benefit for fully 3D PET *IEEE Trans. Med. Imaging* **25** 529–38
- Surti S, Kuhn A, Werner M E, Perkins A E, Kolthammer J and Karp J S 2007 Performance of Philips Gemini TF PET/CT scanner with special consideration for its time-of-flight imaging capabilities *J. Nucl. Med.* **48** 471–80
- Suzuki H, Tomborello T A, Melcher C L and Schweitzer J S 1993 Light emission mechanism of  $\text{Lu}_2(\text{SiO}_4)\text{O}:\text{Ce}$  *IEEE Trans. Nucl. Sci.* **40** 380–3
- van der Laan D J, Schaart D R, Maas M C, Beekman F J and Bruyndonckx van Eijk C W E 2010 Optical simulation of monolithic scintillator detectors using GATE/GEANT4 *Phys. Med. Biol.* **55** 1659–75
- van Loef E V D, Dorenbos P and van Eijk C W E 2001 High-energy-resolution scintillator:  $\text{Ce}^{3+}$  activated  $\text{LaBr}_3$  *Appl. Phys. Lett.* **79** 1573
- van Loef E V D, Dorenbos P, van Eijk C W E, Kraemer K W and Guedel H U 2002 Scintillation properties of  $\text{LaBr}_3:\text{Ce}^{3+}$  crystals: fast, efficient and high-energy-resolution scintillators *Nucl. Instrum. Methods Phys. Res. A* **486** 254–8
- Yang Y, Qi J, Wu Y, James S, St Farell R, Dokhale P A, Shah K S and Cherry S R 2009 Depth of interaction calibration for PET detectors with dual-ended readout by PSAPDs *Phys. Med. Biol.* **54** 433–45
- Zhang J, Olcott P D, Chinn G, Foudray A M K and Levin C S 2007 Study of the performance of a novel 1 mm resolution dual-panel PET camera design dedicated to breast cancer imaging using Monte Carlo simulation *Med. Phys.* **34** 689–702
- Ziegler S I, Ostertag H, Kuebler W K, Lorenz W J and Otten E W 1990 Effects of scintillation collection on the time resolution of a time-of-flight detector for annihilation quanta *IEEE Trans. Nucl. Sci.* **37** 574–9